Chapter VI

Slant Stack Stochastic Inversion

6.1 Introduction

We are now able to apply the theory of chapter 5 directly to the problem of slant stack inversion. As in the case of velocity stacking, the slant stack stochastic inverse is an alternative to the generalized inverse of chapter 3. To justify the use of the parsimony functional $S_P(\mathbf{u})$ of equation (5.43), we must stipulate that the data approximately satisfy the following condition: events in the data have linear moveout. Equivalently, the data set must be the slant stack of a parsimonious function in model space.

This chapter is an extension of chapter 5, for here we shall apply the stochastic inversion method developed in chapter 5 to a vertical seismic profile. The only difference between the method illustrated in this chapter, and the stochastic inversion method of the last chapter, lies in the choice of operator L. Let L now be the slant stack operator defined by equation (2.21):

Slant L:
$$d(h,t) = \int_{-\infty}^{\infty} dp\ u(p, t - ph) \tag{2.21}$$

The inversion algorithm in table 5.1 for the new choice of L remains unchanged. For purposes of comparison, we shall calculate both the generalized inverse (chapter 3) and the stochastic inverse (chapter 5) to the vertical seismic profile.

6.2 Stochastic inversion on a vertical seismic profile

Figure 6.1 illustrates a *VSP (vertical seismic profile)*, courtesy of Arco Oil and Gas Co. Each trace on the profile represents the vertical component of a seismic wavefield, recorded by a geophone from within a well, and generated by a vibrator on the surface 400 feet from the well. In a typical VSP survey there is only one geophone in the well. Between each recording, the geophone is unclamped from the sides of the well bore, pulled up 100 feet or so, and clamped back in place. Thus each trace on the VSP is the wavefield sampled at that depth in the well.

Four distinct families of events are visible on figure 6.1. The strongest events, traveling downward at speeds of 10,000 to 12,000 feet/second, are the direct compressional waves from the source. Barely visible are events with the same velocity as the downgoing waves, but with opposite dip: they are compressional waves reflected from the sedimentary interfaces near the well bore. The direct downgoing and reflected upcoming waves are the events of interest on a VSP, for they provide velocity and reflectivity information on the sediments in the vicinity of the well bore.

The remaining two families of events are up- and downgoing waves with a propagation speed of approximately 5000 feet/second. They are tube waves: interface waves which arise from the presence of the cylindrical interface between the well casing and the borehole fluid. A reflected (upcoming) tube wave can be seen to occur at approximately the 4500 foot level; this is caused by a casing shoe at that depth (DiSiena et. al., 1980). Since these events are restricted almost entirely to within the well bore, they provide no useful information about the surrounding geology, but serve only to mask the direct compressional events.

It would be desirable to filter the tube waves out of the VSP, but this cannot be done directly because of the unfortunate coincidence of aliased tube wave energy with the direct wave energy in the Fourier domain. Let us consider the

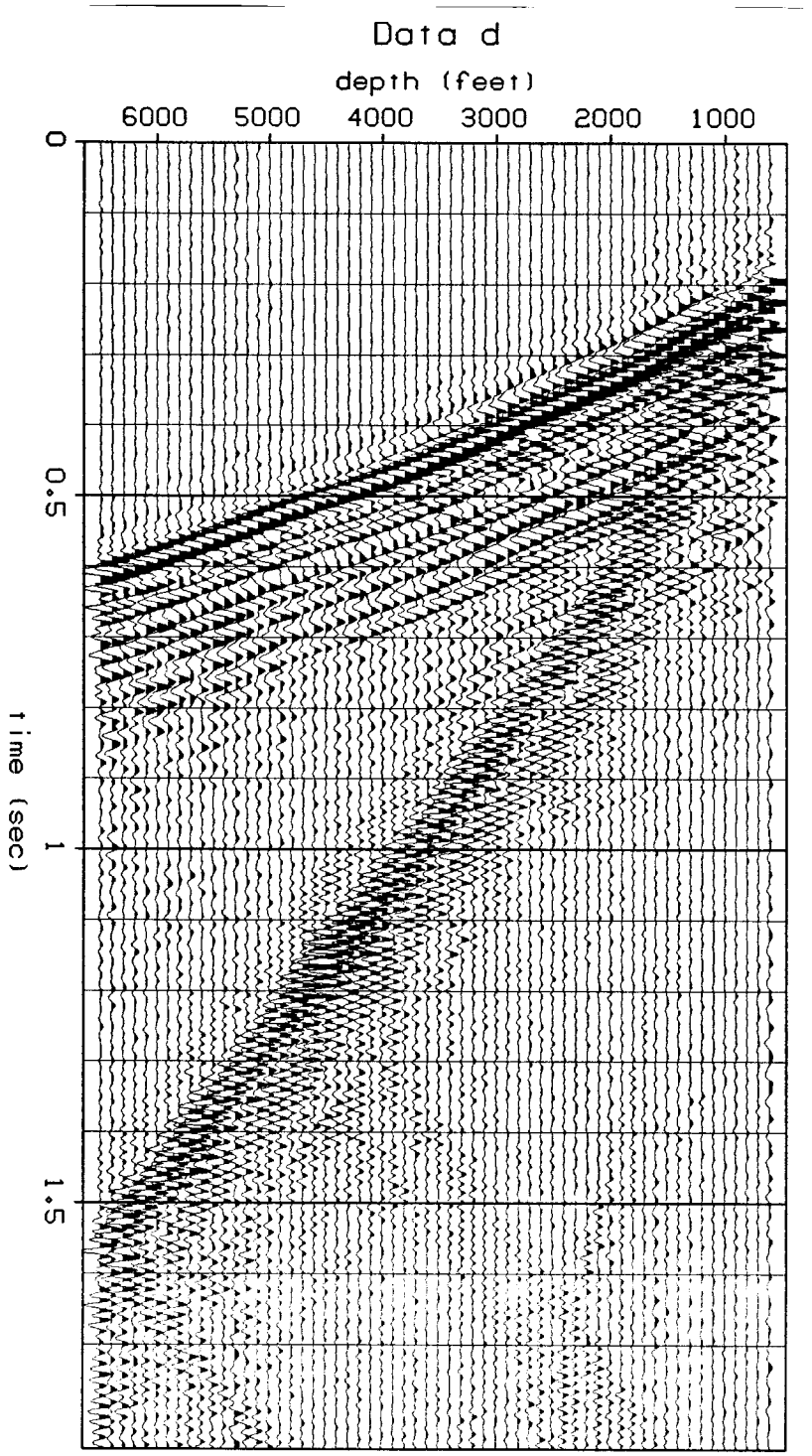

FIG. 6.1. A vertical seismic profile, courtesy of Arco. The depth interval is 100 feet, the time sampling interval is 4 msec. The profile is true-amplitude (i.e. ungained).

aliasing problem in more detail by slant stacking a subset of the VSP, a 2000-foot depth window from 2500 feet to 4500 feet (figure 6.2). Energy on the slant stack clusters, as expected, at slownesses of ± 0.2 msec/foot and ± 1.2 msec/foot, corresponding to the respective velocities of the tube waves and the compressional waves. Unfortunately there is a large amount of overlap between the aliased events of one wave type and the unaliased events of the other wave type.

The aliasing on the slant stack $\mathbf{L}^T\mathbf{d}$ in figure 6.2 is quite strong. This can be seen more clearly by considering the slant stack of a simple synthetic model for $\mathbf{u}$ (figure 6.3). This synthetic model consists of the downgoing direct- and downgoing tube-waveforms sampled, at their true velocities, from the slant stack of figure 6.2. In figure 6.3, the synthetic data set in the center panel was created by slant stacking (with L) the synthetic $\mathbf{u}$ shown on the left panel. The forward stack ($\mathbf{L}^T\mathbf{d}$) of the synthetic data is illustrated on the right panel. Comparing the two stacks $\mathbf{L}^T\mathbf{d}$ on figures 6.2 and 6.3, we see that the pattern of events on the synthetic stack match quite closely the pattern on the real data stack. However it is obvious that all of the energy outside the heavily-outlined boxes on the synthetic stack (figure 6.3) are undesirable artifacts.

The artifacts in figure 6.3 are aliasing artifacts, because they are the direct result of constructive interference between events on the synthetic data panel at dips other than the event's true dip. It is an interesting coincidence that the peaks in the power of the aliased events seem to lie precisely on top of the unaliased events, at the slowness values of ± 0.2 msec/foot and ± 1.2 msec/foot. Vertical seismic profiles are naturally more susceptible to aliasing problems than common-midpoint gathers, because each trace is the wavefield recorded by one geophone in the well. Each trace on a common-midpoint gather is usually the output of an extended geophone or hydrophone array, whose purpose is to filter out precisely those events that might otherwise be aliased on the data.

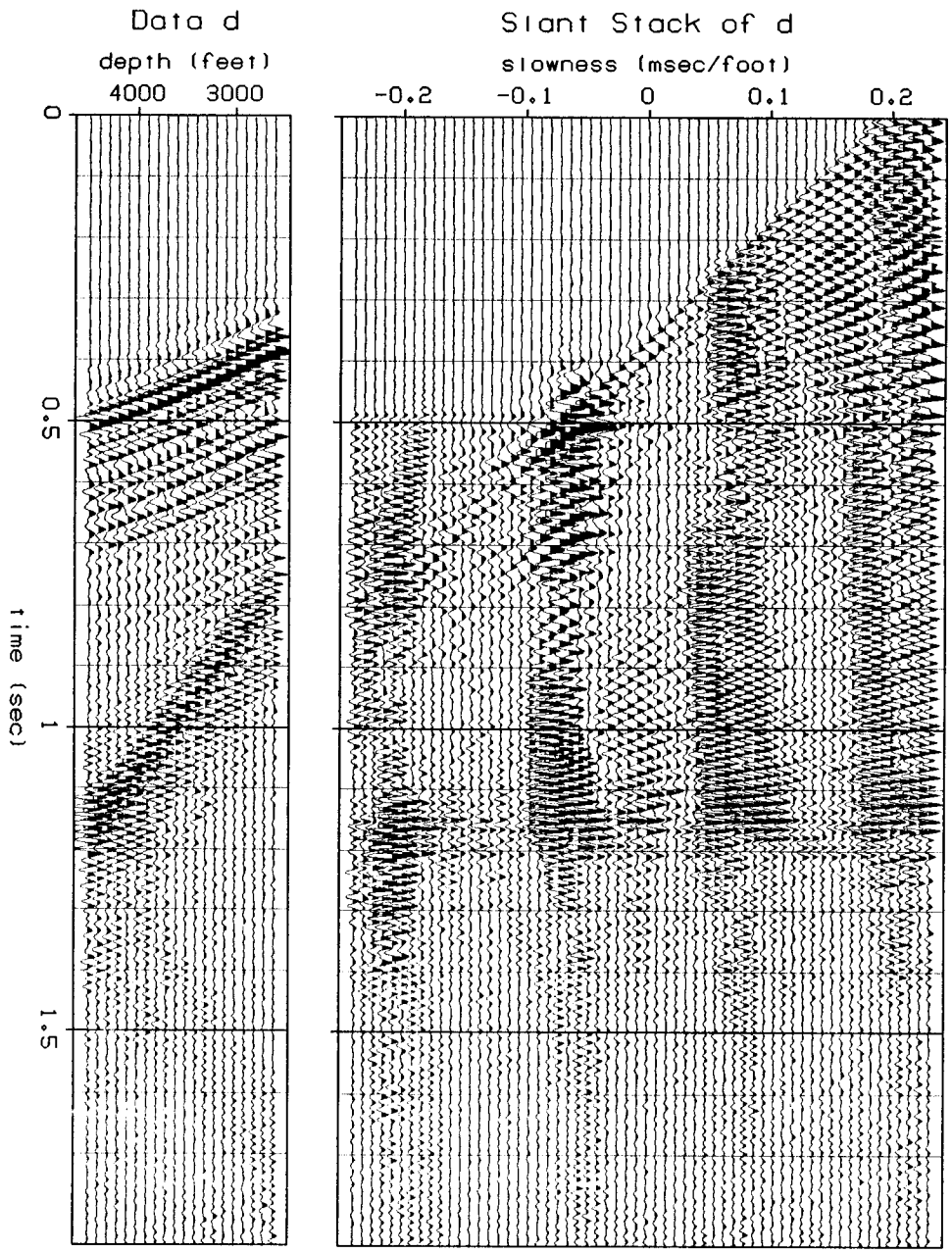

FIG. 6.2. A slant stack of a window of the VSP. The left panel is 21 traces from the vertical seismic profile of figure 6.1, taken from 2500 feet to 4500 feet. The right panel is a slant stack over this window; the slowness interval is 8 usec/foot, and the time sampling interval is 4 msec.

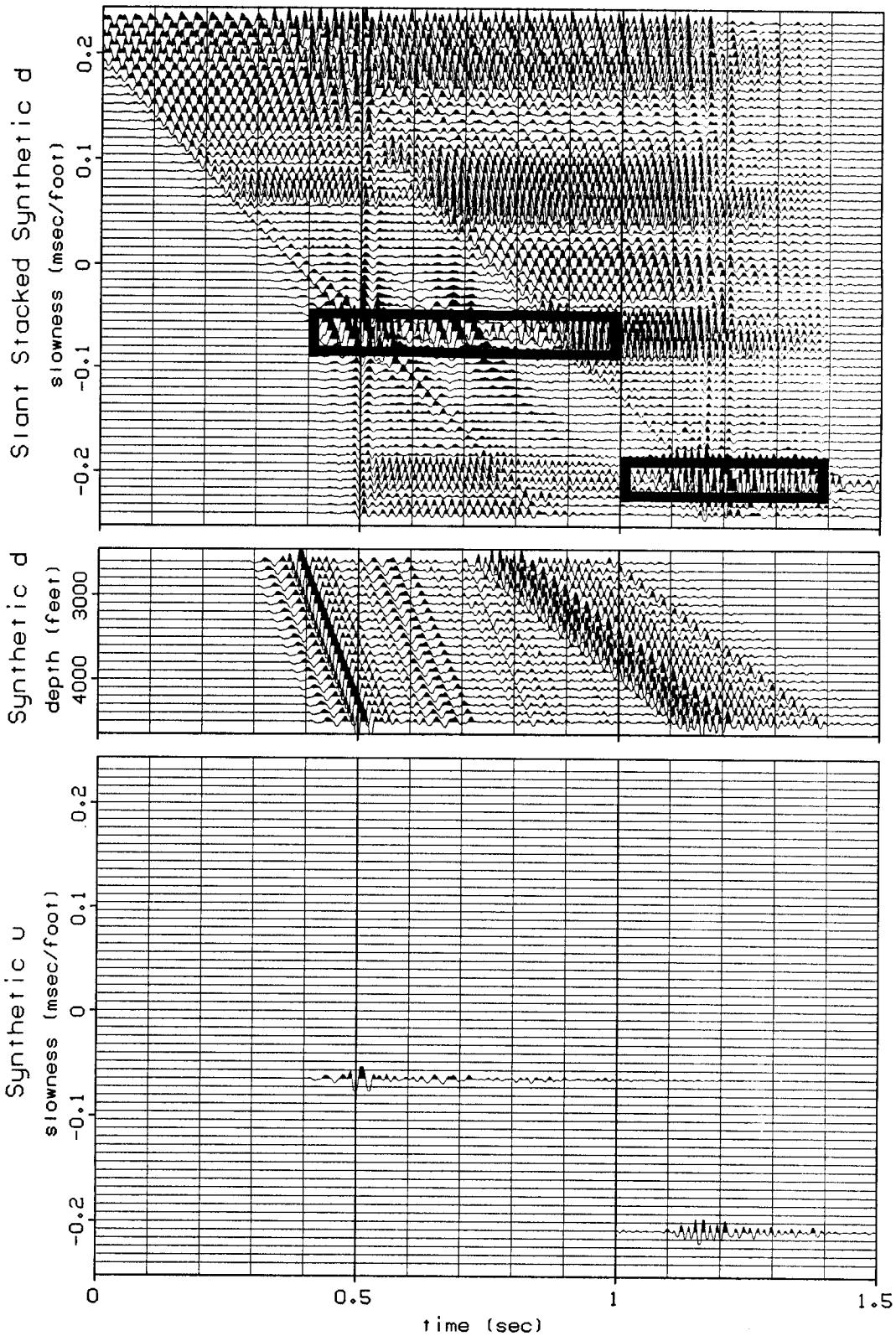

FIG. 6.3. Aliasing artifacts on a synthetic VSP. The left panel is the desired solution **u**; the two nonzero traces in it have actually been pulled from the slant stack of figure 6.2. The central panel shows the resulting synthetic data **d** = **Lu**, analogous to the data of figure 6.2. The right panel is the slant stack, $\mathbf{L}^T\mathbf{d}$, of the synthetic data. The right panel may be compared to the slant stack of figure 6.2. The only "legitimate" events on the slant stack (enclosed in the boxes with the heavy outline) are those which also occur on **u**.

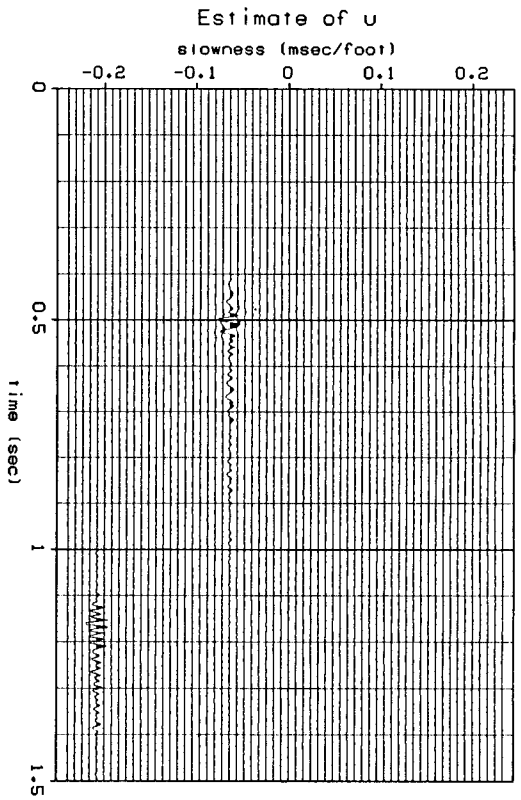

FIG. 6.4. Stochastic inverse of the **synthetic** slant stack. The inverse **u** is the result of applying 20 iterations of the algorithm in table 5.1 to the **synthetic data** of figure 6.3. σ_∞ equals the maximum $|u|$, σ_0 equals $10^{-5}\sigma_\infty$, and σ_n was allowed to float by estimating it at each iteration.

The imaging power of stochastic inversion is demonstrated by the estimated stochastic inverse **u** of the *synthetic* data, shown in figure 6.4. **u** is the result of twenty iterations of the algorithm of table 5.1. The quality of the image speaks for itself; inversion however has a tendency to work perfectly on synthetic data.

Figure 6.5, on the other hand, shows the outcome of twenty iterations of the stochastic inversion algorithm applied to the real data window of figure 6.2. The estimate of **u** is shown on the right in figure 6.5, and the envelope of **u**, i.e., $\boldsymbol{\sigma}(\mathbf{u})$, is shown on the left. In order to compare the behavior of the stochastic inverse method to the generalized inverse method, we apply the generalized inverse (rho filter) developed in chapter 3 to the data. The result is shown in figure 6.6. The

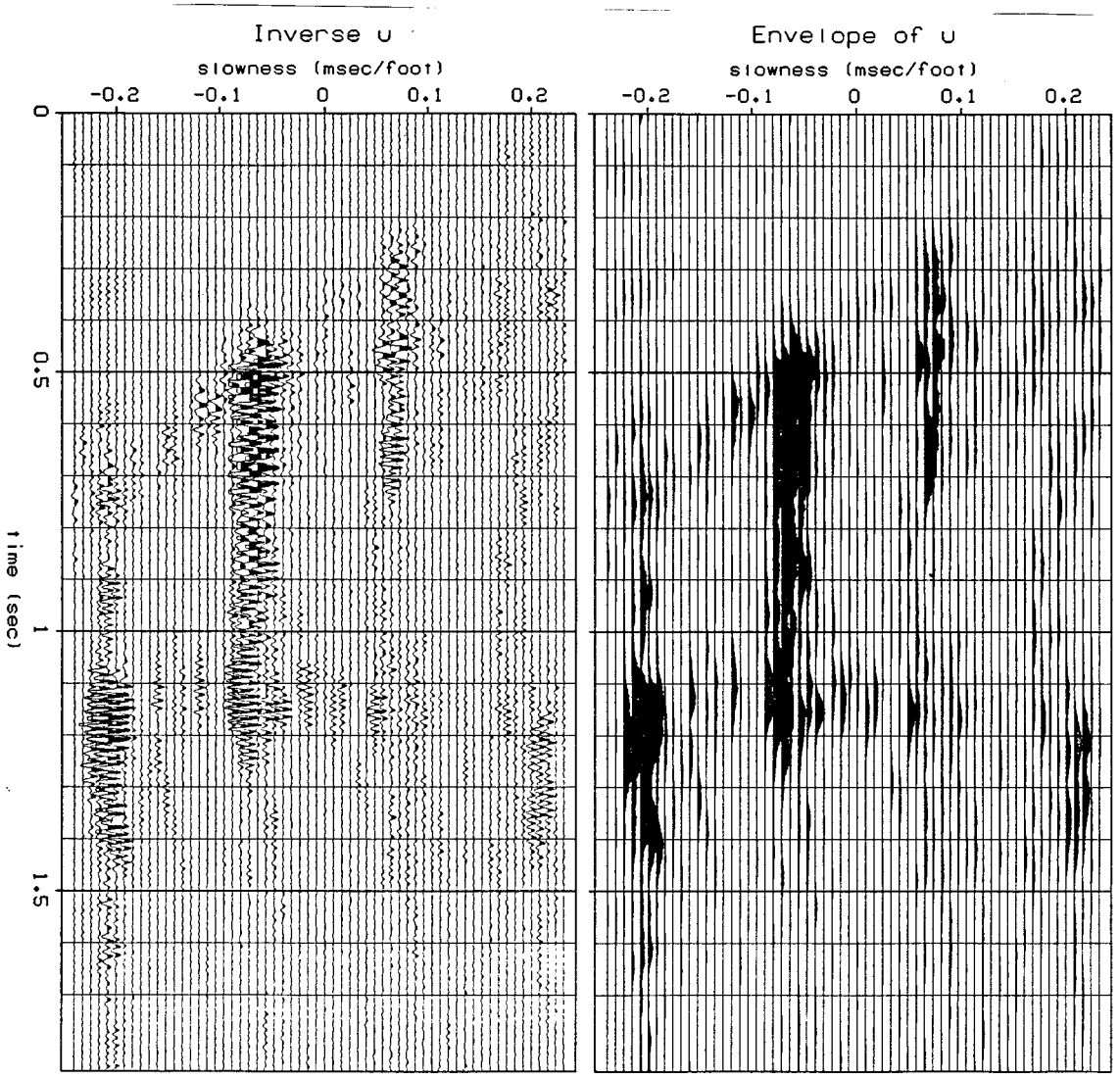

FIG. 6.5. Stochastic inverse of the Arco slant stacked VSP. This **u** is the result of applying 20 iterations of the stochastic inverse algorithm to the **real** data of figure 6.2. The same conventions were used to set σ_∞, σ_o and σ_n as in figure 6.4. The right panel is the estimate of $\boldsymbol{\sigma}(\mathbf{u})$, the variance of **u**.

rho-filtered slant stack, or $(\mathbf{L}^T\mathbf{L})^+\mathbf{L}^T\mathbf{d}$ in the notation of chapter 3, does not seem to have the ability to reduce the aliased noise on the stack. The stochastic inverse has a much greater ability to reduce the aliased power by relegating it to its proper, unaliased location. Yet there remain some events, which we can be certain are artifacts, because of the physical constraints imposed on event velocities in the VSP. The problem seems to be worst over the region near the 1.1 second line on

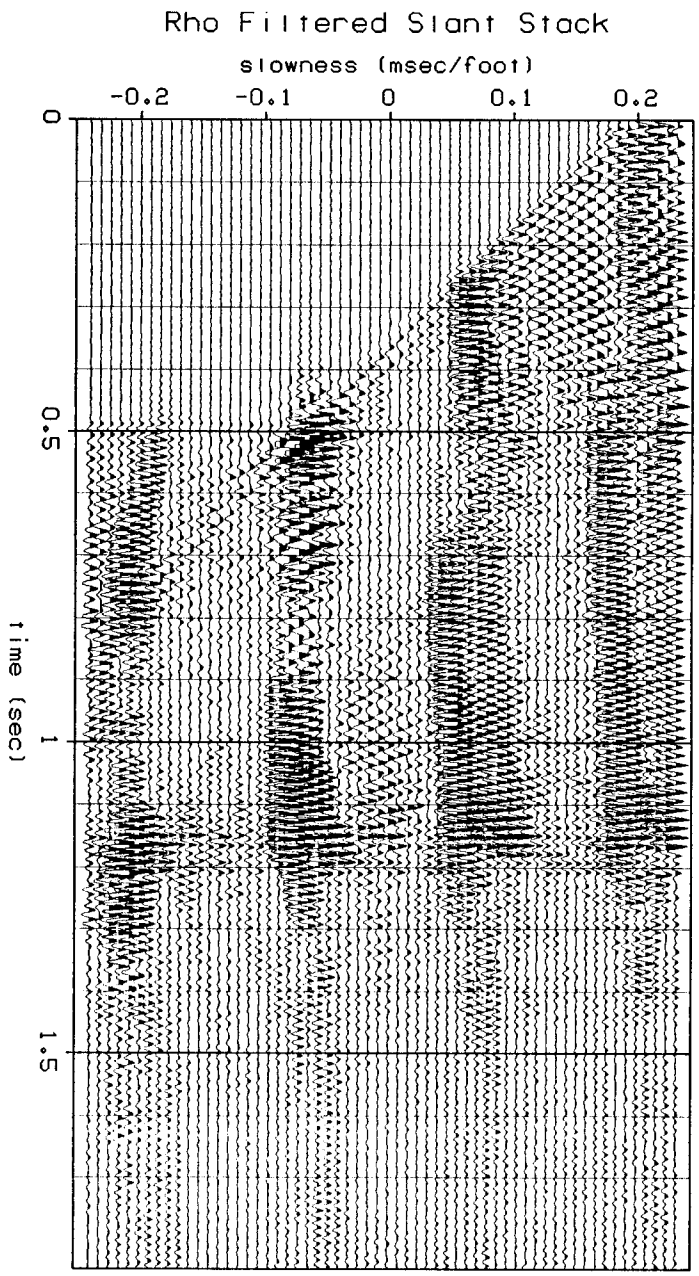

FIG. 6.6. Rho-filtered slant stack. The result of applying the slant stack generalized inverse $(\mathbf{L}^T\mathbf{L})^+$, developed in chapter 3, to the slant stack $\mathbf{L}^T\mathbf{d}$ of figure 6.2.

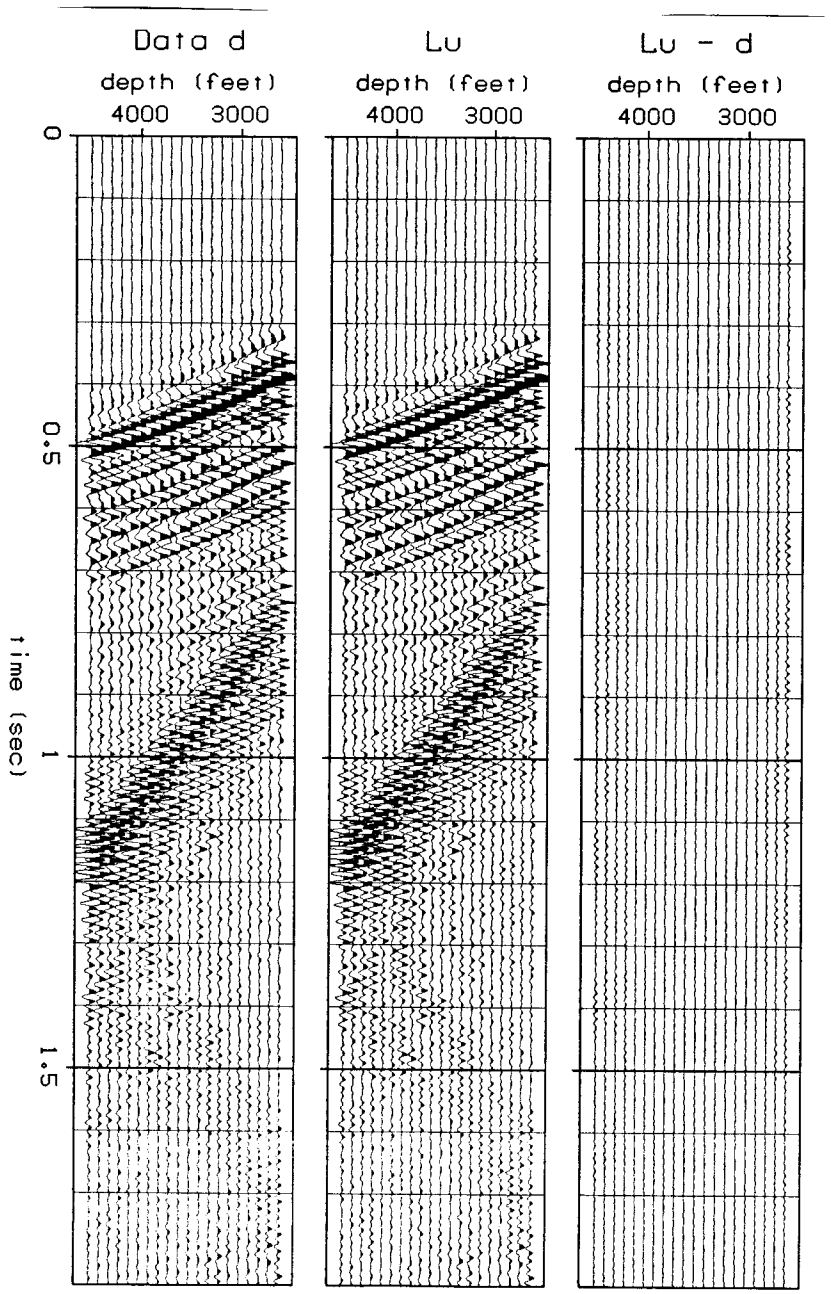

FIG. 6.7. Restoration of one window of the VSP. The center panel is the slant stack **Lu** of the inverse **u** shown in figure 6.5. **Lu** models the data; the data set **d** of figure 6.2 is replotted, for comparison, on the left. On the right is the difference, **Lu** − **d**, between the two.

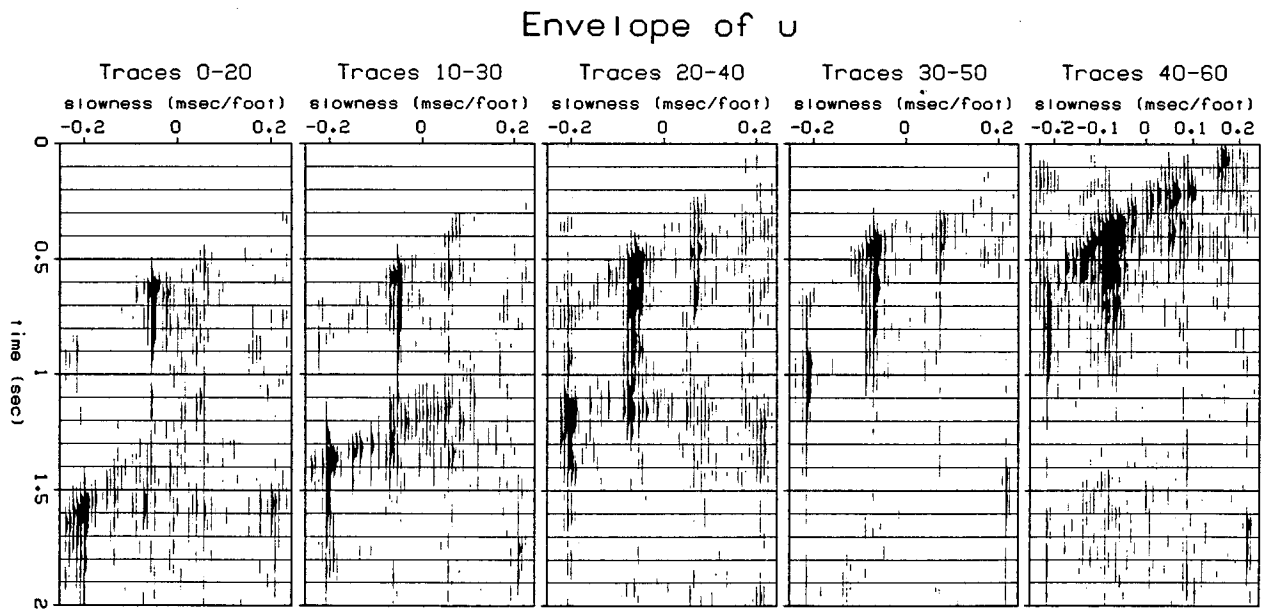

FIG. 6.8. Stochastic inverses of five VSP windows. The VSP of figure 6.1 was divided into five overlapping windows of 21 depth traces each. Traces 0-20 correspond to depths from 6500 to 4500 feet, traces 10-30 from 5500 to 3500 feet, and so on. A separate **u** was determined for each window; the panels shown are the envelopes of each **u**.

the panel **u** in figure 6.5. Nevertheless the ability of the stochastic inverse **u** to model the original data is remarkable. Figure 6.7 compares the original data **d** with the estimated data **Lu**, and with the residual **d** − **Lu**. The fit could hardly be better, considering that **Lu** is the result of 20 iterations on a 15,000-dimensional system of equations.

Compressional events on a VSP are not actually linear because of the characteristic increase in media velocity with depth. The assumption of linear moveout on the events can be made valid if the VSP is divided into a set of overlapping windows in depth. Each window (21 traces wide) was inverted for **u**; the corresponding envelopes of **u** for each window are shown in figure 6.8. From the envelopes we are able to get an idea of how much the energy in model space has focused through n iterations of the algorithm. Twenty iterations on each window seems to be sufficient

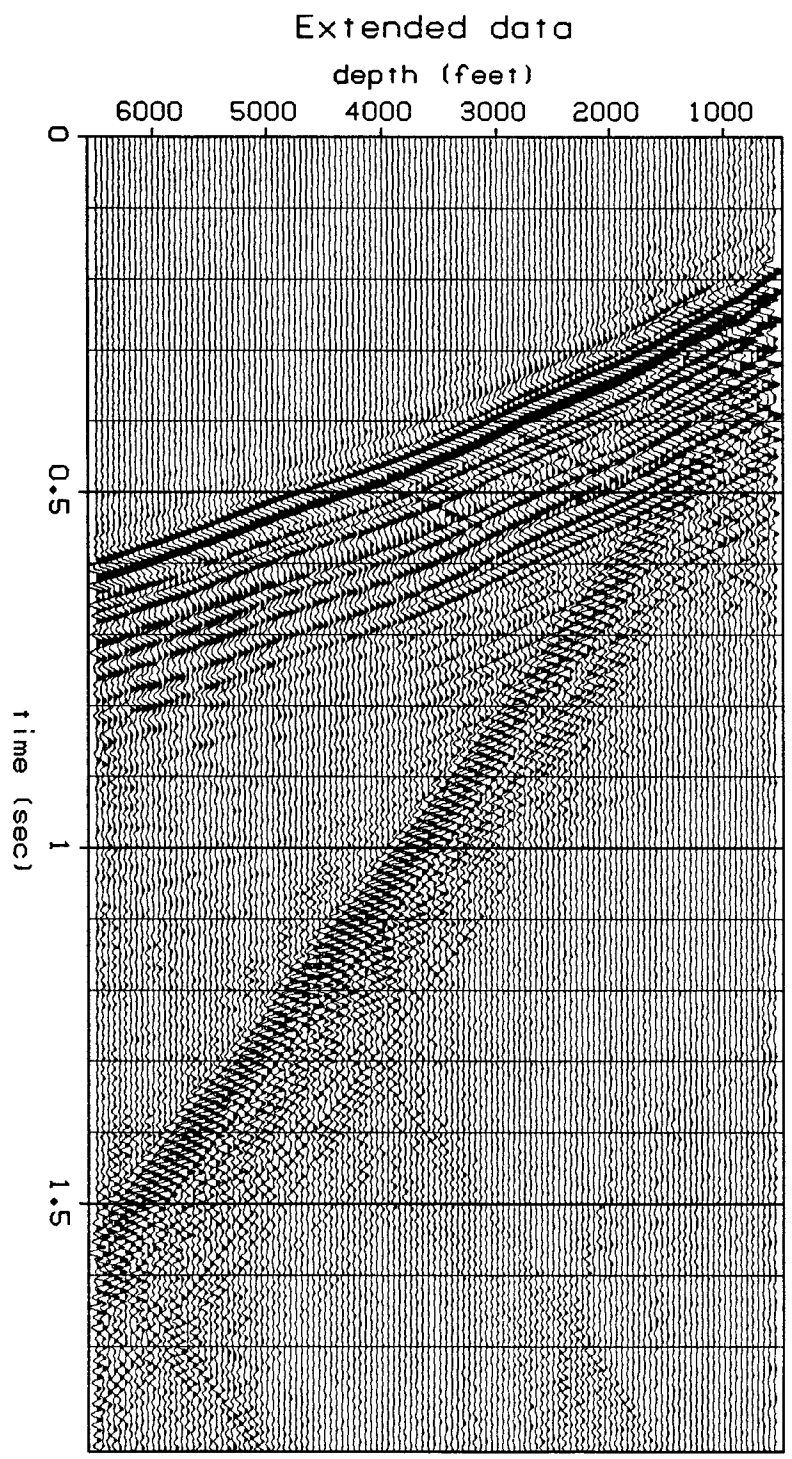

FIG. 6.9. An extrapolated VSP. The estimates **u** of figure 6.8 were slant stacked with an **L** that produced traces at 50 foot depth intervals. This figure is a weighted average of the resultant five overlapping panels **Lu**, with the original traces of figure 6.1 restored. Thus every other trace on the plot has been estimated.

to focus the events in this case.

Finally, figure 6.9 is an example of trace interpolation on the VSP by use of the slant stack inverses of figure 6.8. The interpolated traces (every other trace of figure 6.9 is synthetic) were created by slant stacking each panel **u** over its corresponding data window. Where the windows overlapped, a weighted average was taken to make the trace. The reflected compressional events are more easily traced on the interpolated VSP than on the original VSP, which indicates that the weak reflected events have been interpolated in the presence of the stronger direct compressional events.

This brings to a conclusion the examples of stochastic inversion on a vertical seismic profile. When events in the data domain exhibit linear moveout, the slant stack inverse should be able to cluster sparse events together in the slant stack (model) domain. This justifies the use of a parsimony measure, such as $S_P(\mathbf{u})$ of chapter 5, whose gradient can be used to force the inverse to be sparse. Though the transformation L from model space to data space in this chapter differs from the L of chapter 5, the same parsimony functional and the same algorithm were used to get an approximate inverse $\mathbf{u} = \mathsf{L}^{-1}\mathbf{d}$ to the data.

finis